Determining tool/chip temperatures from thermography measurements in metal cutting

M. Saez-de-Buruaga[a], D. Soler[a], P. X. Aristimuño[a], J. A. Esnaola[a], P. J. Arrazola[a]

[a] *Manufacturing Department, Faculty of Engineering-Mondragon Unibertsitatea, Mondragon, Spain*

Abstract

Temperature measurement in metal cutting is of central importance as tool wear and surface integrity have been demonstrated to be temperature dependent. In this context, infrared thermography is presented as a reliable technique to determine tool temperatures and thermal fields at near real-time. However, a constraint of this technique is that temperatures are measured on the tool side faces normal to the cutting edge but offset from the tool/chip contact.In the present research, tool/chip contact temperatures were calculated from the tool side based on analytical theories of heating and the principles of heat generation in cutting processes. The required inputs were commonly measurable variables (cutting and feed forces, chip thickness and tool/chip contact length). The proposed approach was combined with a new calibration method in which a calibration curve that directly relates real and radiated temperatures is obtained, instead of measuring the emissivity of the radiating surface.

As a case study, the research was conducted on a set of four ferrite-pearlite steels (16MnCr5, 27MnCr, C45 and C60). The results demonstrated the effectiveness of the method to establish the real influence of the cutting conditions (cutting speed and feed) and to distinguish the effect that different work material microstructures have in tool/chip temperature. Furthermore, the results showed a high degree of accuracy and less than 12% deviation from the trends when compared with 2D cutting simulations.

Keywords: Temperature Measurement, Infrared Thermography, Metal Cutting, Orthogonal Cutting

1. Introduction

The experimental investigation of heat generation occurring in metal cutting has received much attention in recent decades [1], as it is well established that tool-chip interface temperatures have significant influence on machining performance. Problems such as tool wear are commonly linked to activation temperatures above which diffusive mechanisms cause exponential reduction of tool life [2]. Even the surface integrity of machined components is affected by the temperatures reached during processing [3]. Basically, these cutting temperatures are an indirect measurement of heat produced due

Email address: msaez@mondragon.edu (M. Saez-de-Buruaga)

to the high plastic deformation of the material, and tool/chip and tool/workpiece friction [4].

Temperature measurement techniques can be mostly divided into direct and indirect methods. Indirect techniques have the drawback of only giving post-process information of the maximum temperatures reached during cutting [5, 6]. The most extensively used direct method is the tool/work thermocouple. However, it has limited transient response, does not effectively obtain accurate temperature gradients and interferes with heat flow [7, 8].

Another direct method is infrared thermography (IR), which has become a matured and widely accepted condition monitoring tool where the temperature is measured in a non-contact manner [9]. This non intrusive technology has the benefit of not interfering with heat flow as other methods such as thermocouples do, and also enables the direct determination of temperature fields in near real-time. However, it has some drawbacks such as difficulties in measuring temperatures when the presence of dust or water vapor is found in the environment, as these absorb the emitted radiation of the object. In fact, due to the difficulty of using IR techniques for measuring temperature with lubricants [10], dry orthogonal cutting is the only choice considered in nearly all research works. Another drawback is the establishment of an appropriate methodology to obtain accurate measurements [11, 12], and the cost of the equipment.

The accuracy of all known infrared techniques depends on the calibration technique employed, which essentially is linked to the estimation of the emissivity [13]. The emissivity of an object depends on factors such as temperature, measuring angle, geometry of the surface and constitution of the surface (polished, oxidized, rough, sandblasted). Therefore, this is commonly the major uncertainty source [12] in IR measurements. To solve this problem, researchers have developed calibration methods in which real temperature values from camera response are directly obtained without the need for emissivity correction [14].

Most research works focus their analysis on the measurement of tool temperatures, although researchers have also attempted to measure those of the chip/workpiece [15]. However, the curl occurring in the chip and the swelling of the chip and workpiece as a consequence of thermal expansion, leads to a lack of control of the topology of the measured surface. Thus, measuring radiation on non-flat surfaces may lead to considerable uncertainties on given temperatures.

When focusing on tool temperature measurements, the major challenge is to estimate those occurring in the tool/chip or tool/workpiece contact area. During cutting, the chip obstructs a clear view of the tool, which is reported as one of the principal disadvantages of IR techniques to measure tool/chip interface temperatures [16, 17]. In order to prevent this problem three alternatives can be found in the literature, (i) modify tools by drilling holes to allow partial vision of the tool-chip interface [18], (ii) place the camera orthogonally to the chip flow, allowing the measurement of the temperature on a side face of the tool [19, 20] or (iii) use transparent tools [21, 22]. Although the knowledge acquired in these studies is valuable, the fact that the materials and geometry of the tools employed do not correspond to those of real cutting operations, may lead to significant changes in the thermal fields.

Another option is that published by [23], who developed a methodology to directly record rake face temperatures when orthogonal cutting a Ti-alloy and AISI 4140 steel. However, as reported by [14], the observed tool temperatures did not correspond exactly

to those that occur during the cutting operation, as cooling occurs when the chip moves away and the rake face becomes visible. The authors thus assumed that temperatures during the cut would be at least 150-200°C greater than those measured, and the location of the measured maximum temperature might not correspond with the real location when cutting.

The researchers of [24] proposed an alternative to calculate tool/chip contact temperatures from measured tool side temperatures, in which the camera was placed orthogonally to the chip flow. Based on classical theories of heating, they developed an equation to calculate the temperature increase depending on the distance from the contact to the tool side (overhang distance). The authors demonstrated the technical feasibility of the developed methodology, as the temperature rises corresponded to previously developed tests of their own property. However, in spite of the reliability of the results, the main inputs required for the calculations such as the heat flux produced by friction effects or even the heat partition between tool and workpiece were roughly estimated.

Taking into account that the studies in the literature still have certain weaknesses, a new approach was developed in this research for the establishment of tool/chip contact temperatures. The first step was to experimentally measure IR temperatures in the tool side, following the studies of [11], as the direct measurement of the temperatures on the rake face presented some uncertainties due to cooling/quenching effects. The real tool side temperatures were obtained from radiation temperatures based on the method proposed by [14]. In this method, a calibration curve that relates real and radiated temperatures is obtained, which eliminates the need for calculating the emissivity of the radiating surface.

The main innovation of the present research occurs in the second step. In this step, tool side temperatures are transferred to those of the tool/chip contact, combining the theory proposed by [24] with the shear plane model of [25] for the calculation of heat fluxes generated when cutting.

The study was conducted on four different ferrite-pearlite steels: 16MnCr5, 27MnCr5, C45 and C60. These work materials were selected to cover a wide range of microstructure variants of commonly employed steels in the development of automotive products such as camshafts, gear wheels and pinions. In the manufacturing route of these components, machining processes such as turning, broaching and drilling are commonly employed operations. The goal was to determine to what extent the improvement of the methodology proposed in this paper distinguished the influence of microstructure in the tool/chip contact temperature.

The contribution of the proposed methodology is that it determines the real influence of cutting conditions on cutting temperatures, which then permit a reliable comparison between all the tested steels. In addition, the accuracy of the method was also compared with a set of 2D cutting simulations, where calculated and simulated tool/chip contact temperatures obtained a low degree of deviation and the same trends.

This article is structured as follows: first the description of the materials, the experimental and calibration procedures and the analytical theories to transfer tool side to tool/chip contact temperatures is presented in the methodology section. Then, the main results are presented, in which tool side and tool/chip contact temperatures are analyzed. In the next section, the compliance of the results with those of literature and simulations are discussed and finally, the main conclusions from the research work are presented.

2. Methodology

2.1. Workpiece materials

Four different ferrite-pearlite steel grades were selected to develop this research: 16MnCr5, 27MnCr5, C45 and C60. These were selected to cover a wide range of microstructure variants. All the grades were processed by isothermal annealing, in order to obtain a ferrite-pearlite structure as homogeneous as possible. The chemical composition of the different grades is summarized in Table 1.

Table 1: Chemical composition of steel grades

Grade	C	Si	Mn	S	P	Ni	Cr	Mo	Cu	Al
16MnCr5	0.19	0.17	1.23	0.028	0.016	0.19	1.03	0.07	0.17	0.020
27MnCr5	0.25	0.24	1.19	0.033	0.009	0.09	1.06	0.04	0.11	0.032
C45	0.45	0.33	0.78	0.025	0.014	0.09	0.12	0.02	0.11	0.007
C60	0.61	0.28	0.65	0.027	0.016	0.14	0.11	0.04	0.24	0.005

Microstructure data and mechanical properties are given in Table 2. The ferritic and pearlitic grain sizes were qualitatively measured following the standard ASTM E112-13 by means of the intercept method. Tensile and hardness tests were carried out to determine the mechanical properties.

Table 2: Microstructure properties: ferrite-pearlite ratio (%ferrite/%pearlite), ferritic and pearlitic grain size (µm). Mechanical properties: yield strength (YS-MPa), ultimate tensile strength (UTS-MPa) and Brinnel hardness (HB)

	16MnCr5	27MnCr5	C45	C60
%ferrite / %pearlite	58 / 42	40 / 60	25 / 75	14 / 86
size ferrite / size pearlite	10 / 15	14 / 15	17 / 22-27	11 / 31
YS (MPa)	306	367	361	372
UTS (MPa)	544	610	667	699
Hardness (HB)	162	163	185	188

2.2. Experimental cutting procedure

The experimental procedure was designed for fundamental variable measurement in an orthogonal tube. The employed set-up is detailed in previous publications [11]. The setup was mounted on a CNC vertical milling machine as shown in Figure 1. The tool and tool holder were clamped on a dynamometer (Kistler 9121) to measure cutting and feed forces. These and the infrared (IR) camera (FLIR Titanium 550M) were fixed on the moving table of the machine-tool. The orthogonal cutting specimens in tubular form were held on the spindle, which gave the rotation movement and the vertical feed. These specimens were of 58±0.05 mm diameter and 2±0.02 mm wall thickness (width of cut).

A ground surface was machined on the inserts to generate a perpendicular surface for IR measurements, enabling the capture of the thermal field on a side face of the tool. This tool side was placed at an offset distance (d, overhang distance) from the tool/chip

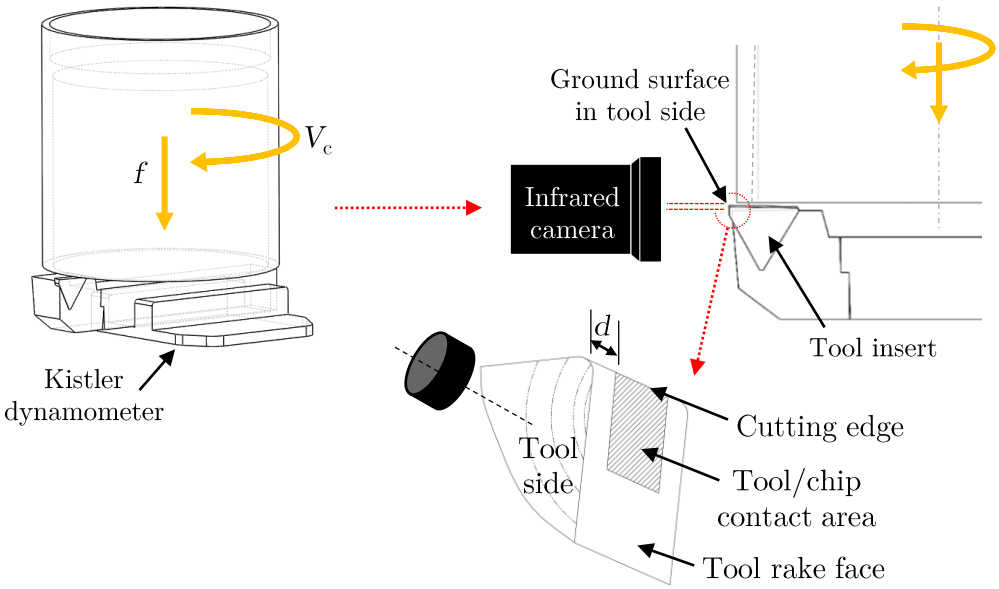

Figure 1: Schematic representation of the orthogonal cutting methodology. Identification of the measured tool side temperature, and the region to calculate the too/chip contact temperature

contact area. To control the overhang distance, every time a new insert was placed in the tool holder, the positioning of the ground face of the insert was referenced with a Renishaw MA2-LP2 probe. After each test, the overhang distance was measured by both a Leica Z16 APO macroscope and an Alicona Infinite Focus G4 profilometer. Chips were also collected during tests to analyze the chip morphology.

Tests were developed in four different cutting conditions (cutting speeds of 100-200 $m \cdot min^{-1}$ and feeds of 0.1-0.2 mm). Due to the limitations of measuring tool temperatures with an IR camera, the tests were constrained to dry cutting conditions. To simplify the study, an uncoated P25 grade carbide (WIDIA TPUN-160308-TTM) was selected to develop the whole test matrix. For each tested condition and material, at least three repetitions were carried out to determine the uncertainty of results.

The process parameters and output variables of these orthogonal cutting experiments are summarized in Table 3 and Table 4 respectively.

To evaluate the chip thickness, the cross section of the chips was analyzed. Chips were etched, ground and polished, and micrographs were captured with a Leica DM-IR microscope. An example of a micrography is shown in Figure 2-a. To evaluate the contact length, the contact patterns on the rake face of the tool were measured with an Alicona Infinite Focus G4. An example of a capture from the profilometer is shown in Figure 2-b.

Table 3: Process parameters utilized in orthogonal tests

Machine & Cutting Tools	Machine tool	Vertical CNC Milling machine
	Tool holder	WIDIA - CTGPR2020K16
	Insert Tool reference	WIDIA - TPUN160308TTM
	Grade	P25
	Coating	No
	Clearance Angle	6°
	Rake Angle	5°
	Tip radius	0.4 mm
	Cutting edge radius	40 µm
Workpiece	Geometry	Orthogonal tube
	Material	16MnCr5, 27MnCr5, C45, C60
	Condition	Isothermal annealed
Cutting Conditions	Operation	Orthogonal turning
	Cutting speed	100-200 m·min^{-1}
	Feed	0.1-0.2 mm
	Depth of cut	2 mm

Table 4: Output variables measured in orthogonal tests

Fundamental variables	Cutting force	Kistler 9121 dynamometer
	Feed force	Kistler 9121 dynamometer
	Tool temperature	FLIR Titanium 550 IR camera
	Chip thickness	Leica DM IRM microscope
	Contact length	Alicona Infinite Focus G4

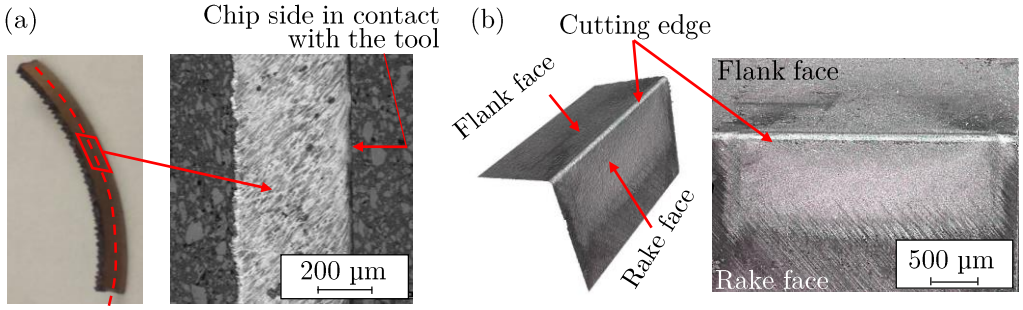

Figure 2: (a) Example of chip thickness and (b) contact length measurements for C45 steel machined at V_c=200 m·min^{-1} and f=0.2 mm

2.3. Infrared camera calibration procedure

In the present study, the new calibration method published in [14] was employed, directly relating radiation temperature (expressed in Digital Levels - DL) with real temperature (T) without the need for emissivity correction. This methodology results in an interpolating function of (DL,T) that inherently includes the emissivity of the radiating

surface.

The used setup for calibration heats tool inserts up to 1000°C in a controlled argon atmosphere. It consists of a hermetic box, inside which a clamping system for tool inserts is placed. An induction system heats the insert to the desired temperatures, and is controlled with two thermocouples placed on the measured surface. Tool temperatures are recored with the IR camera, placed perpendicular to the surface of the insert on a positioning table. In this procedure the calibration is performed under the same experimental conditions (integration time-IT, optical path, field of view) as those used during the cutting process. This eliminates the introduction of new uncertainty sources.

It is worth noting that there was a difference on the heating rate of the insert between the machining experiments (1000 °C·s^{-1}) and the calibration set-up ($1-10$ °C·s^{-1}). This involved that, in real machining experiments the tool side did not oxidize as the insert was heated in periods of less than 5 s. In contrast, the time required during calibration to reach the desired temperatures would make the insert to oxidize if no argon was employed. To prevent the tool from oxidation and have heating conditions similar to those of the machining process, an argon inlet was fixed into the hermetic box, in which the level of oxygen was controlled with a LuminOx SST sensor.

The calibration procedure was applied to characterize the insert WIDIA TPUN-160308-TTM. This was calibrated on the two ITs employed in the IR measurements of the orthogonal tests, 60 and 100 µs. The resultant data and fitted polynomials are shown in Figure 3. The obtained results showed a deviation in the range of 3-5% between the two repetitions that were carried out for each of the ITs. The fitted polynomials are presented in Eq. 1 and Eq. 2.

$$T_{\mathrm{IT60}} = 8.15 \cdot 10^{-9} DL^3 - 5.74 \cdot 10^{-5} DL^2 + 0.22\, DL + 129.13 \tag{1}$$

$$T_{\mathrm{IT100}} = 1.51 \cdot 10^{-9} DL^3 - 1.93 \cdot 10^{-5} DL^2 + 0.13\, DL + 127.16 \tag{2}$$

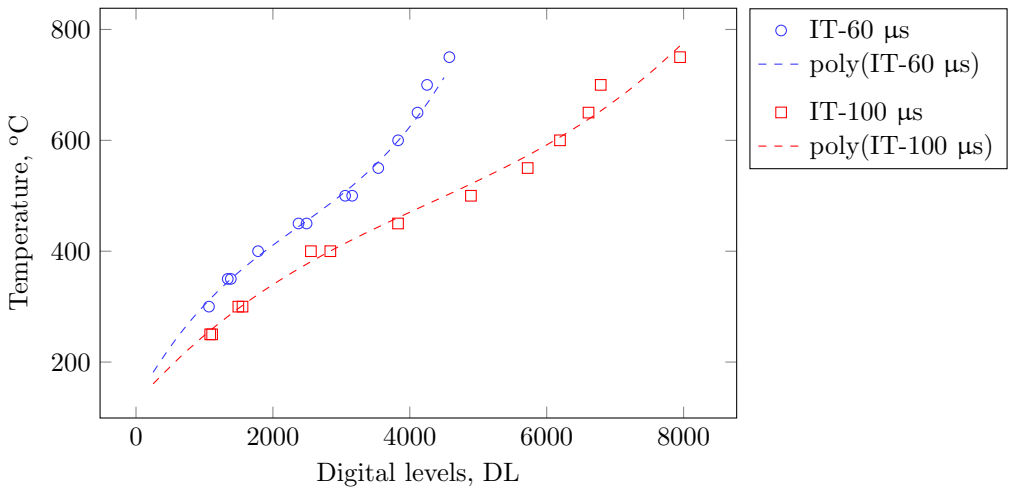

Figure 3: Experimental data and fitted polynomials of (T, DLs) for each employed IT

2.4. Analytical theory to estimate tool/chip contact temperature

To better understand the physics occurring in the tool/chip interface, measured tool side temperatures were extrapolated to the mid-plane of the contact section. The methodology was defined in two steps. The first consisted of calculating the heat flux generated due to shear stresses on the rake face (q_{tool}). The second step was applied to calculate the increase in temperature that belongs to the overhang distance (d). The analytical equations to calculate this value require as input data the previously calculated heat flux. This is schematically described in Figure 4.

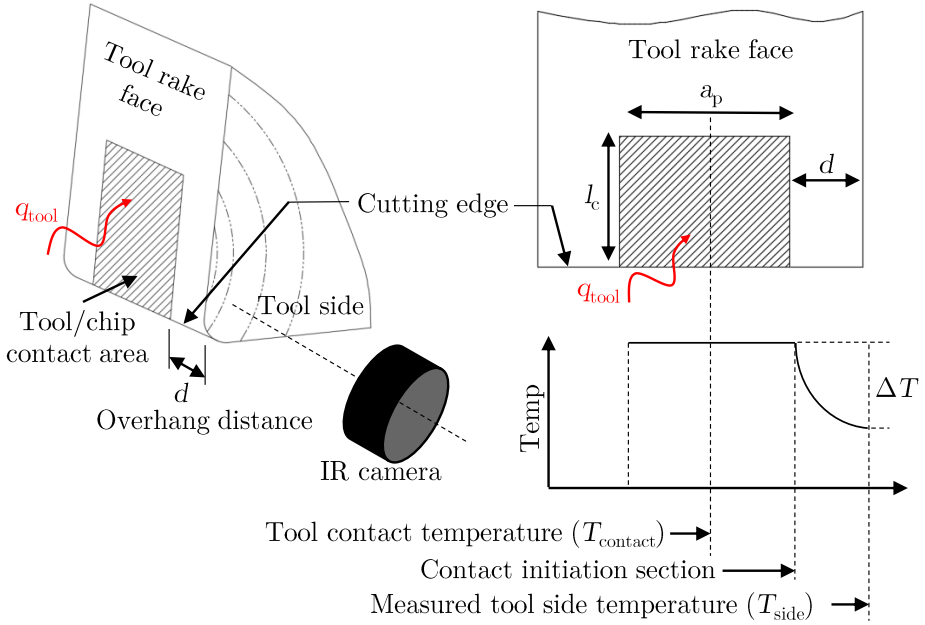

Figure 4: Extrapolation method from tool side to mid-plane contact temperature

Supposing that the tool has a perfectly sharp cutting edge, F_c could be attributed to the normal stresses on the rake face, and F_f to the shear stresses on the rake face. It was assumed that with fresh tools no stresses occur on the flank face.

The heat flux on the rake face, which is in turn the heat flux of the secondary shear zone (q_{sh2}), was calculated based on the shear plane model [25]. The corresponding friction angle (λ in Eq. 3) and the shear plane angle (ϕ in Eq. 4) were calculated based on the static component of the cutting forces (F_c and F_f) and chip thickness (t_2).

$$\lambda = \gamma + \text{arctg}\left(\frac{F_f}{F_c}\right) \tag{3}$$

$$\phi = \text{actg}\left(\frac{\frac{t_1}{t_2}\cdot\cos\gamma}{1-\frac{t_1}{t_2}\cdot\sin\gamma}\right) \tag{4}$$

The resultant shear forces on the rake (F_{sh2}) were calculated by translating the cutting and feed forces to the tangent and normal directions with respect to the rake face.

$$F_{\mathrm{sh2}} = F_c \cdot \sin\gamma + F_f \cdot \cos\gamma \tag{5}$$

The shear stresses on the secondary shear zone (τ_{sh2}) were obtained with Eq. 6 in which F_{sh2} was divided by the effective contact area, which was calculated by Eq. 7.

$$\tau_{\mathrm{sh2}} = \frac{F_{\mathrm{sh2}}}{A_{\mathrm{sh2}}} \tag{6}$$

$$A_{\mathrm{sh2}} = a_{\mathrm{p}} \cdot \frac{t_1 \cdot \sin\left(\phi + \lambda - \gamma\right)}{\sin\phi \cdot \cos\lambda} \tag{7}$$

The heat flux on the SSZ was obtained with Eq. 8.

$$q_{\mathrm{sh2}} = \tau_{\mathrm{sh2}} \cdot V_{\mathrm{chip}} = \tau_{\mathrm{sh2}} \cdot V_{\mathrm{c}} \cdot \frac{t_1}{t_2} \tag{8}$$

Once the heat fluxes on the secondary shear zone (SSZ) were calculated, the amount of friction or shear heat that flows into the tool was determined by the heat partition (α^* in Eq. 9). It is usually assumed that approximately 3-10% of the friction heat is transferred to the tool [4, 24].

$$q_{\mathrm{tool}} = \alpha^* \cdot q_{\mathrm{sh2}} \tag{9}$$

The correction methodology based on the analytical model proposed by [24] was used to correct the influence of the overhang distance. To apply this model some assumptions were also made. First, the analytical model calculates the rise in temperature generated by a unique heat flux on a rectangular surface of a semi-infinite solid, not the coupled effect of two heat fluxes acting on two adjacent surfaces of a body (the heat fluxes on the rake and flank faces). For this reason, the rise in temperature in the rake was assumed to be independent from that of the flank, considering that heat fluxes do not interfere with each other, and with unworn tools the heat flux in the flank is much lower than that of the rake face. This model has also the implicit assumption that the temperature throughout the tool/chip contact area is constant, which means that the temperature at the beginning of the contact is considered the same as that of the mid plane (see Figure 4).

The analytical equation proposed by [24] is presented in Eq. 10. Based on the classical theories of heating, it estimates the temperature rise ΔT at an overhang distance (d) from the tool side. The input parameters required to calculate ΔT are the contact length (l_{c}), the heat flux (q_{tool}) and the conductivity of the tool (measured K_{tool}=112-18 W·m^{-1}·K^{-1} at 20-800°C).

$$\begin{aligned}\Delta T = \tfrac{2q_{\mathrm{tool}}}{\pi K_{\mathrm{tool}}} l \Big[1 - \tfrac{d/a_{\mathrm{p}}}{l/a_{\mathrm{p}}} \sinh^{-1}\left(\tfrac{l/a_{\mathrm{p}}}{d/a_{\mathrm{p}}}\right) \\ + \sinh^{-1}\left(\tfrac{d/a_{\mathrm{p}}+1}{d/a_{\mathrm{p}}}\right) - \sinh^{-1}\left(\tfrac{d/a_{\mathrm{p}}}{l/a_{\mathrm{p}}}\right) \Big]\end{aligned} \tag{10}$$

3. Results

The main results of the measurements of temperature on the tool side (T_{side}) and the calculated tool/chip contact temperatures are described in this section. The results of required fundamental variables to calculate the temperature increase from the tool side to the mid-plane of the tool/chip contact section (ΔT) are described in Appendix A. Specifically, these latter are the chip thickness, contact length, cutting forces and feed forces (see Table A.5).

3.1. Measured tool side temperature

Before the analysis of results, it should be noted that tool side temperatures when orthogonal cutting the C45 and C60 samples were recorded with an overhang distance of d=0.3 mm, while in the tests of the 16MnCr5 and 27MnCr5 this had to be increased to d=0.5 mm. This modification in the overhang was necessary to avoid the obstruction that the severe workpiece lateral side flow was generating between the camera and the tool side in the latter two steels. As a consequence, the T_{side} between the steels was not comparable, as the overhang distance is known to significantly affect temperature measurements [24].

The T_{side} corresponds to the maximum temperature measured on the tool. This is located on the rake face marked on the thermal field of Figure 5-a. The temperatures showed an increasing trend during the orthogonal cutting process up to a certain value, above which the temperature became stable. Once the temperature stabilizes, the process is commonly considered under steady state, and thus temperatures are considered to be constant throughout the rest of the process. This is clearly observed in Figure 5-b, in which the evolution of rake temperature over time is plotted for the example case of a C45 steel.

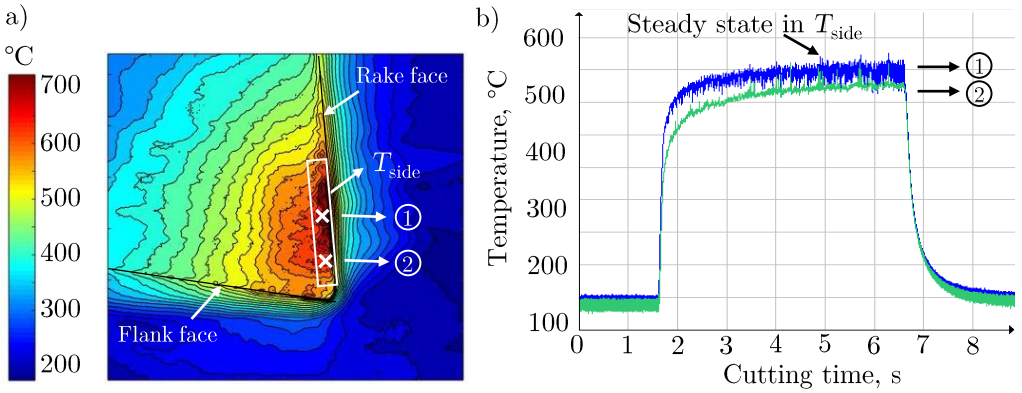

Figure 5: a) Thermal field of tool side and b) evolution of temperature on the rake face for a C45 steel machined at V_c=200 m·min^{-1} and f=0.2 mm

The solid columns of the plot in Figure 6 correspond to the results of T_{side}. In general, the maximum temperatures measured on the rake face achieved a maximum value of 575°C. It can be assumed that the influence that cutting conditions had on T_{side} was not affected by the different overhangs employed. Therefore, it was calculated that

increasing both the cutting speed and feed generated an average increase of 18% and 14% respectively on T_{side}.

3.2. Tool/chip contact temperature

Contact temperatures were calculated based on the approach presented in Section 2. These were calculated as the sum of $T_{\text{contact}} = T_{\text{side}} + \Delta T$. In the calculations, the heat partition was set to $\alpha^* = 4\%$ based on the works of [4, 24].

3.2.1. Analysis of calculated temperature rise (ΔT) from T_{side} to T_{contact}

Both, T_{side} and calculated T_{contact}, are depicted in Figure 6. The solid section of the columns in the plot correspond to the measurements of T_{side}, and the hatched section depicts the calculated temperature rises (ΔT). The error bars of the solid columns correspond to the standard deviation of the experimental measurements of T_{side}. The error bars of the hatched columns are the sum of these latter, plus the deviation obtained in the calculation of ΔT due to the intrinsic deviation of the variables involved in the equations (F_c, F_f, l_c, t_2). The error of the predicted ΔT was found in the range of 10-45°C, which once added to the deviation of the empirical measurements, gave a total deviation of 30 to 80°C. However, the maximum deviation was always lower than 7-10% of the given T_{contact}.

The values of ΔT were in the range of 130-395°C, which compared to that of T_{side}, means an increase in temperature of 30-75%. The greatest values were obtained at high

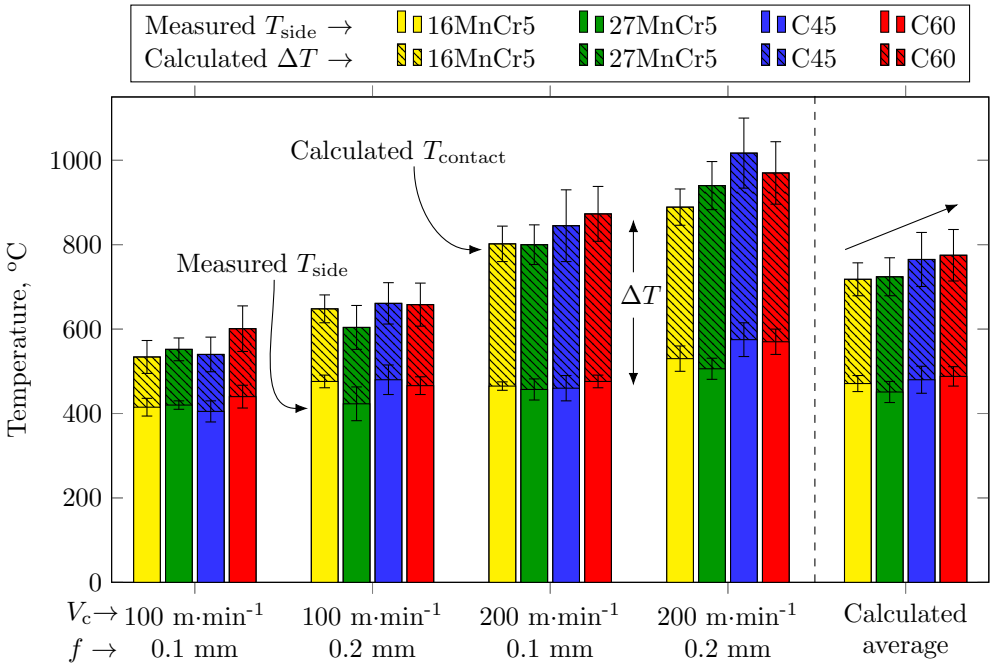

Figure 6: Measured tool side temperatures and calculated tool/chip contact temperatures for each cutting condition, and average values of temperature

cutting speeds and feeds. Unexpectedly, the greatest ΔT was achieved in the case of C45, followed in decreasing order by the C60, 27MnCr5 and 16MnCr5. However, the overall differences in ΔT between steels were of less than 10%.

3.2.2. Calculated contact temperature

In general, based on the average T_{contact} values plotted in Figure 6, it was determined that the C60 steel achieved the highest contact temperatures, followed in decreasing order by the C45, 27MnCr5 and 16MnCr5. However, this trend was not always followed, as in certain cutting conditions the T_{contact} of C45 was greater than that of the C60. A similar occurrence was observed when comparing the 16MnCr5 and 27MnCr5.

The maximum T_{contact} of 1015°C was achieved when cutting the C45 at V_{c}=200 m·min^{-1} and f=0.2 mm. At this cutting condition, the maximum difference in T_{contact} between the steels was 130°C. The minimum temperature of 530°C was obtained at V_{c}=100 m·min^{-1} and f=0.1 mm in the case of 16MnCr5. At this latter condition, the difference between the steels was less than 65°C.

From the point of view of the influence that cutting conditions had on T_{contact}, increasing the cutting speed from 100 to 200 m·min^{-1} caused an average temperature rise of 40%, while the effect of modifying the feed from 0.1 to 0.2 mm caused an increase of 15%. The results suggest that duplicating the cutting speed was more sensitive to T_{contact} increase, compared to the effect of duplicating the feed.

4. Discussion and compliance with literature

In general, the results of chip thickness were in line with the literature. Steels with a higher ferrite content achieved thicker chips, increasing cutting speed provoked a reduction of chip thickness and increasing the feed reduced the chip thickness ratio [6, 26, 27].

Globally, in the present research increasing ferrite content provoked an increase in l_{c}, which is also in line with previous studies [6].

In the literature review diverse trends were found in cutting force results when cutting ferrite-pearlite steels. Some authors concluded that increasing pearlite content involved in increase in F_{c} [28], while others concluded almost the opposite [6]. In this research no differences beyond the measurement uncertainties in K_{sc} were found between the steels. When the tool has no wear, cutting forces are commonly linked to normal pressures on the rake face [25], and the contact area which is defined by the contact length (l_{c}) and the width of cut (a_{p}). Taking into account that the steels with higher ferrite content achieved longer l_{c}, in spite of their lower strength and possibly lower normal pressures, their F_{c} or K_{sc} was the same as the C45 and C60 steels. With regards to the results of K_{sf}, the greater values measured in the steels with higher ferrite content were in line with the literature [6, 29].

In the case of the calculated ΔT, the close values obtained when comparing the calculated temperature rises of the 16MnCr5 and 27MnCr5 to the C45 and C60 are worth noting (see the ΔT values depicted in Figure 6). However, this was to be expected as the analytical equations developed by [24] predicted greater temperature rise as the overhang distance (d) increases, which is the case of 16MnCr5 and 27MnCr5.

It is also important to note the lower ΔT achieved in the C60 compared to C45, in spite of being studied with the same overhang. However, taking into account that

the applied analytical equations depend on l_c, the lower predicted temperature rise in the case of C60 was reasonable as the l_c of this steel was shorter than that of the C45. In general, the calculated temperature rises were greater than those estimated by [24], who stated that temperatures on the tool side could be underestimated by 30% when compared to those of the contact. In the case of this research a significantly higher $\Delta T/T_{side}$ of up to 75% was calculated.

The calculation of ΔT also made it possible to discern the influence of the microstructure in tool/chip temperatures ($T_{contact}$). Although a greater difference in the average temperatures between steels was expected (see Figure 6), it was possible to determine that the increase in pearlite content caused an increase in $T_{contact}$. It needs to be highlighted that the results of T_{side} were less sensitive to the influence of microstructure. For example, the measured average temperature of the 27MnCr5 was lower than that of the 16MnCr5, while this was expected to be the opposite.

One of the most significant results of this research was the variation which occurred in the effect that cutting conditions had on tool temperature when switching from T_{side} to $T_{contact}$. When only T_{side} was analyzed, the influence of cutting speed and feed did not differ much. In contrast, when the analysis was focused on $T_{contact}$, the influence of both cutting speed and feed became more significant, with cutting speed showing a difference in rates of up to 40% and the latter of up to 15%. Comparing these results with those found in the literature, the cutting speed is commonly identified as the cutting parameter that most affects tool temperature. For example, [6] observed that varying the feed from 0.1 to 0.2 mm when machining a low alloyed steel may generate a increase of approximately 10%, while increasing the cutting speed from 100 to 200 m·min^{-1} had an influence of 20%. These findings suggest that the analysis carried out in this study with regards to $T_{contact}$ better describe the thermal behavior during cutting.

For an extended analysis, the calculated $T_{contact}$ were also compared with those extracted from a FEM model of the cutting process. The model was that described by [30], in this case set-up in Abaqus/Explicit (v6.14). This was employed to obtain qualitative information of tool/chip interface temperatures during cutting. The coupled mechanical and thermal analysis was done using the Arbitrary Lagrangian Eulerian (ALE) formulation. Although the purpose of the modeling developments are primarily for discussion, the main properties are given in Table B.6 and a short description of the model is done

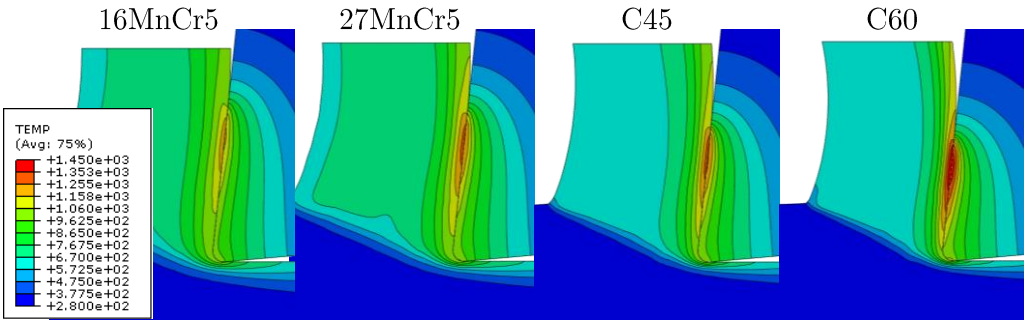

Figure 7: (a) Temperature comparison between all tested ferrite-pearlite steels when simulated at V_c=200 m·min^{-1} and f=0.2 mm.

in Appendix B so as to ensure the reliability of given results.

Figure 7 illustrates the steady state temperature distribution in the chip for the tested steels when machined at V_c=200 m·min^{-1} and f=0.2 mm. Note the particularly refined mesh applied in the tool edge contact in order to counteract the large gradients of the variables analyzed in this area.

The comparison of the maximum temperatures between the simulation and the experiments is shown in detail in Figure 8. These correspond to those experimental and analytically calculated T_{contact} on the rake face which are described in Figure 6.

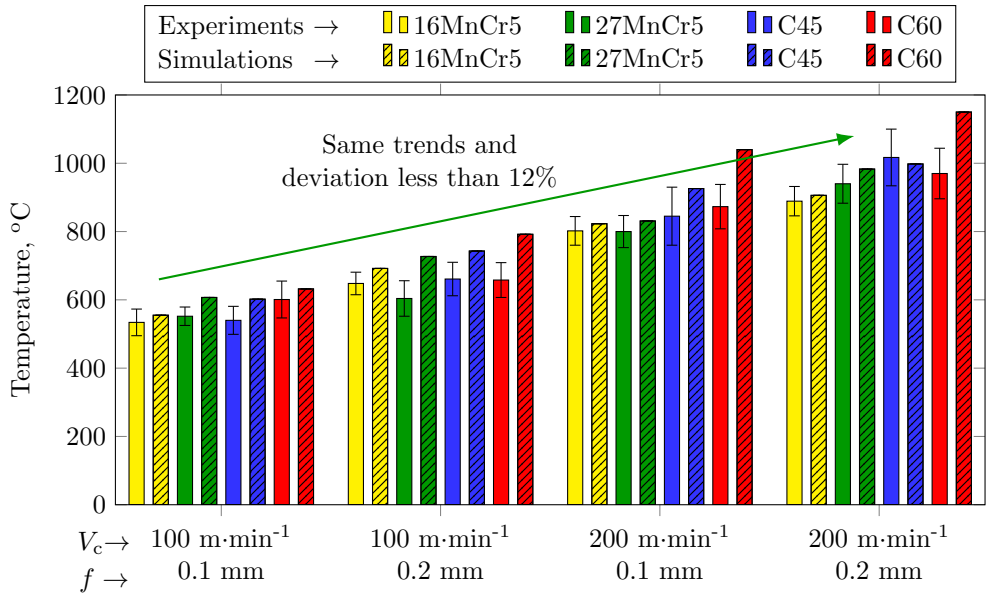

Figure 8: Experimental and simulation results of T_{contact} on the rake face for all the FP steels and cutting conditions machined with fresh tools

In general terms, calculated temperature results were in line with those simulated, as a good qualitative agreement was observed in the main trends. While in the experiments the effect of increasing feed and cutting speed caused an average temperature rise of 38% and 14% respectively, in the case of the simulations the corresponding effect was 35% and 15%. With regards to the specific temperature values, the maximum deviations were less than 18%, while the average error was less than 12%. From the abovementioned results, it was possible to conclude that the calculated temperatures were able to represent the temperatures in the tool with a high degree of accuracy.

5. Conclusions

An approach was established to calculate tool/chip contact temperatures based on measured tool side temperatures and fundamental variables of cutting and feed forces, chip thickness and contact length. Using the proposed method the real impact that cutting conditions (cutting speed and feed) had on tool/chip temperature is obtained,

which enabled the determination the influence of microstructure when cutting 16MnCr5, 27MnCr5, C45 and C60 ferrite-pearlite steels.

With regards to the influence of the microstructure, it was observed that contact temperatures differed in the same manner as those of the tool side when cutting at 100 $m \cdot min^{-1}$. However, with increased cutting speed, at 200 $m \cdot min^{-1}$, the differences between steels were more appreciable when focusing on calculated contact temperatures. It is important to highlight that the average values of T_{contact} showed that increasing pearlite content caused an increase in tool/chip temperatures. When the comparison was made with regards to the tool side, no relevant conclusions could be achieved concerning the effect of the microstructure.

Temperature corrections in the range of 120-440°C were calculated to overcome the effect of the offset between the tool side and the tool/chip contact area (the overhang distance). Prior to this analysis, these calculated temperature rises when compared to those of the tool side where estimated to be about 30%. However, in the present research it was demonstrated that these could reach up to 75%.

Of further interest is the greatest change observed between T_{side} and T_{contact} when analyzing the influence of the cutting conditions. Due to the greater sensitivity of temperature change when analyzing T_{contact}, it was possible to determine that increasing the cutting speed caused an increase of 40% in temperature, while increasing the feed provoked an increase of 15%. This variation in temperature can not be observed if the analysis is only focused on the temperatures on the tool side, highlighting the importance of calculating contact temperatures.

Thus, the comparison of tool/chip temperatures not only linked the pearlite (or ferrite) content of the steels with the tool/chip temperature, but also enabled the establishment of the temperatures occurring during cutting with reduced uncertainty.

Furthermore, the proposed methodology presented a high degree of accuracy in the comparison with orthogonal cutting 2D simulations. Calculated tool/chip contact temperatures obtained less than 12% of deviation when compared with temperatures from the simulations, and both frameworks followed the same trends. Indeed, less than 3% of deviation was achieved in the prediction of the effect that cutting conditions had on tool/chip contact temperatures.

Acknowledgements

This work was supported by the projects IMMAC (RFSR-CT-2014-00020), MICRO-MAQUINTE (PI_2014_1_116) and EMULATE (DP12015-67667-C3-3R).

Glossary

Symbols:

α^*	Heat partition between tool and workpiece (%)
γ	Rake angle (°)
λ	Friction angle (°)
μ	Friction coefficient (-)
ϕ	Shear angle (°)
σ_0	Lattice friction (MPa)

σ_s	Saturation stress (MPa)
τ_{sh2}	Shear stresses in the secondary shear zone (MPa)
a_{p}	Depth of cut (mm)
A	Strength coefficient (MPa)
A_{sh2}	Effective contact are in the secondary shear zone (mm^2)
B	Thermal sensitivity coefficient in MSB model (-)
C	Strain rate sensitivity coefficient (-)
D	Temperature related empirical constant in strain rate equation (-)
d	Overhang distance (mm)
f	Feed (mm)
F_{c}	Cutting force (N)
F_{f}	Feed force (N)
F_{sh2}	Shear forces in the secondary shear zone (N)
K_{tool}	Thermal conductivity of the tool ($\mathrm{W{\cdot}m^{-1}{\cdot}K^{-1}}$)
K_{sc}	Specific cutting force ($\mathrm{N{\cdot}mm^2}$)
K_{sf}	Specific feed force ($\mathrm{N{\cdot}mm^2}$)
l_{c}	Contact length (mm)
m	Temperature sensitivity coefficient (-)
n	Strain hardening coefficient (-)
q_{sh2}	Heat flux in the secondary shear zone (W)
q_{tool}	Heat flux flowing into the tool (W)
r	Temperature related exponent
t_1	Uncut chip thickness (mm)
t_2	Chip thickness (mm)
t_{eq}	Chip thickness ratio (-)
T	Temperature (°C)
T_{contact}	Temperature in the mid-plane of the contact section (°C)
T_{side}	Temperature on the side of the tool (°C)
V_{c}	Cutting speed ($\mathrm{m{\cdot}min^{-1}}$)
V_{chip}	Chip velocity ($\mathrm{m{\cdot}min^{-1}}$)

Abbreviations:

ALE	Arbitrary Lagrangian Eulerian
DL	Digital levels
FEM	Finite element method
IR	Infrared
IT	Integration time
YS	Yield strength
SSZ	Secondary shear zone
UTS	Ultimate tensile strength

Appendix A. Results of fundamental variables

In order to enable a comparison between the tests at different uncut chip thickness, the chip thickness results are presented in terms of chip thickness ratio, t_{eq} (Eq. A.1). The results of cutting and feed forces were also converted to specific cutting and feed forces, being K_{sc} and K_{sf} respectively (Eq. A.1). These two latter were calculated as the average forces once the steady state was reached.

$$t_{eq} = \frac{t_2}{t_1};\ K_{sc} = \frac{F_c}{t_1 \cdot a_p};\ K_{sf} = \frac{F_f}{t_1 \cdot a_p} \tag{A.1}$$

Table A.5: Measured fundamantal variables to enable the calculation of $T_{contact}$

	V_c m·min^{-1}	f mm	K_{sc} MPa	K_{sf} MPa	t_{eq} -	l_c mm
16MnCr5	100	0.1	3070 ± 100	2735 ± 70	4.23 ± 0.1	0.76 ± 0.18
	100	0.2	2425 ± 25	1825 ± 25	3.17 ± 0.1	0.99 ± 0.13
	200	0.1	2640 ± 40	2150 ± 50	3.18 ± 0.1	0.75 ± 0.05
	200	0.2	2125 ± 10	1335 ± 25	2.71 ± 0.03	0.85 ± 0.45
27MnCr5	100	0.1	3000 ± 40	2685 ± 70	3.82 ± 0.1	0.65 ± 0.1
	100	0.2	2325 ± 35	1690 ± 25	3.02 ± 0.07	1.14 ± 0.06
	200	0.1	2600 ± 20	2095 ± 20	3.05 ± 0.05	0.68 ± 0.07
	200	0.2	2125 ± 40	1315 ± 45	2.45 ± 0.05	0.92 ± 0.06
C45	100	0.1	2805 ± 50	2120 ± 120	3.20 ± 0.1	0.43 ± 0.07
	100	0.2	2345 ± 50	1445 ± 75	2.57 ± 0.03	0.82 ± 0.09
	200	0.1	2585 ± 35	1780 ± 140	2.46 ± 0.15	0.55 ± 0.03
	200	0.2	2135 ± 55	1125 ± 40	2.06 ± 0.07	0.77 ± 0.05
C60	100	0.1	2925 ± 105	2045 ± 35	2.93 ± 0.15	0.53 ± 0.17
	100	0.2	2375 ± 65	1300 ± 55	2.40 ± 0.12	0.72 ± 0.1
	200	0.1	2675 ± 95	1735 ± 35	2.36 ± 0.12	0.47 ± 0.02
	200	0.2	2250 ± 105	1110 ± 15	2.20 ± 0.06	0.68 ± 0.06

Appendix B. Properties of the FEM model

An ALE model was set in Abaqus/Explicit, following the study of [30]. The material behavior was determined by the constitutive model proposed by [31] (see Eq. B.1), in which parameters of the tested steels were characterized with experimental dynamic compression tests. The Coulomb friction law governs mechanical aspects at the tool/chip interface contact in the sliding regime. The friction was defined as being dependent on the sliding velocity between tool and workpiece based on the works of [32, 33]. The values of friction were set in between μ=0.8-0.55 for sliding velocities in the range of 10-300 m·min^{-1}. Heat transfer was allowed at the tool-chip contact section. Following the method proposed by [34], the thermal properties for both tool and workpiece were characterized as functions of temperature, and are presented in Table B.6.

Table B.6: Input parameters related to workpiece and tool material

		16MnCr5	27MnCr5	C45	C60
Young modulus, E (MPa)			$210 \cdot 10^3$		
Poisson coefficient, υ			0.3		
Inelastic heat fraction, β			0.9		
Plasticity	σ_0	276	260	275	265
	σ_s	830	877	960	1017
	A	483.7	536.5	589.9	649.8
	n	0.2714	0.2332	0.1903	0.1259
	r	3.1024	2.5562	1.7983	0.2808
	m		0.0084		
	B		913.6		
	C		1.0033		
	D		0.00115		
Density, ρ ($\mathrm{kg \cdot m^{-3}}$)	20°C	7800	7795	7765	7830
	300°C	7720	7715	7685	7745
	700°C	7570	7565	7535	7600
Conductivity, K ($\mathrm{W \cdot m^{-1} \cdot K^{-1}}$)	20°C	52.6	36.5	32.2	30.8
	300°C	0.4	38.3	34.3	28.8
	700°C	30.7	24.1	20.7	14.4
Specific heat, C_p ($\mathrm{J \cdot Kg^{-1} \cdot K^{-1}}$)	20°C	365	375	395	430
	300°C	515	500	545	530
	700°C	825	745	800	590
Thermal expansion, α_L ($10^{-6} \cdot \mathrm{^oC^{-1}}$)	20°C	5.5	6.5	5.5	4.75
	300°C	12.9	12.5	12.9	12.6
	700°C	14.9	14.9	14.8	14.6

$$
\begin{aligned}
&\sigma = \sigma_\varepsilon(\varepsilon) \cdot \sigma_T(T) \cdot \sigma_{\dot{\varepsilon}}(\dot{\varepsilon}, T) \\
&\sigma_\varepsilon = \sigma_\mathrm{s} + (\sigma_0 - \sigma_\mathrm{s} + A\varepsilon^n)\exp(-r\varepsilon) \\
&\sigma_T = \tfrac{1}{1+e^{-m(T-B)}} \\
&\sigma_{\dot{\varepsilon}} = 1 + (C \cdot D^T) \cdot \ln(\tfrac{\dot{\varepsilon}}{\dot{\varepsilon_0}})
\end{aligned}
\tag{B.1}
$$

References

[1] M. Davies, T. Ueda, R. M'saoubi, B. Mullany, A. Cooke, On the measurement of temperature in material removal processes, CIRP Annals-Manufacturing Technology 56 (2) (2007) 581–604.

[2] H. Takeyama, R. Murata, Basic investigation of tool wear, Journal of engineering for industry 85 (1963) 33.

[3] I. Jawahir, E. Brinksmeier, R. M'Saoubi, D. Aspinwall, J. Outeiro, D. Meyer, D. Umbrello, A. Jayal, Surface integrity in material removal processes: Recent advances, CIRP Annals-Manufacturing Technology 60 (2) (2011) 603–626.

[4] T. Childs, Metal machining: theory and applications, Butterworth-Heinemann, 2000.

[5] S. Rossetto, U. Koch, An investigation of temperature distribution on tool flank surface, Annals of the CIRP (19) (1970) 551–557.

[6] E. M. Trent, P. K. Wright, Metal cutting, Butterworth-Heinemann, 2000.

[7] H. Ay, W.-J. Yang, Heat transfer and life of metal cutting tools in turning, International Journal of Heat and Mass Transfer 41 (3) (1998) 613–623.

[8] D. Stephenson, Tool-work thermocouple temperature measurements theory and implementation issues, Journal of Manufacturing Science and Engineering 115 (4) (1993) 432–437.

[9] S. Bagavathiappan, B. Lahiri, T. Saravanan, J. Philip, T. Jayakumar, Infrared thermography for condition monitoring–a review, Infrared Physics & Technology 60 (2013) 35–55.

[10] M. Cuesta, P. Aristimuño, A. Garay, P. Arrazola, Heat transferred to the workpiece based on temperature measurements by ir technique in dry and lubricated drilling of inconel 718, Applied Thermal Engineering 104 (2016) 309–318.

[11] P. Arrazola, I. Arriola, M. Davies, A. Cooke, B. Dutterer, The effect of machinability on thermal fields in orthogonal cutting of aisi 4140 steel, CIRP Annals-Manufacturing Technology 57 (1) (2008) 65–68.

[12] M. A. Davies, H. Yoon, T. Schmitz, T. Burns, M. Kennedy, Calibrated thermal microscopy of the tool–chip interface in machining, Machining science and technology 7 (2) (2003) 167–190.

[13] P. Herve, J. Cedelle, I. Negreanu, Infrared technique for simultaneous determination of temperature and emissivity, Infrared Physics & Technology 55 (1) (2012) 1–10.

[14] D. Soler, P. Aristimuo, M. S. de Buruaga, A. Garay, P. Arrazola, New calibration method to measure rake face temperature of the tool during dry orthogonal cutting using thermography, Applied Thermal Engineering 137 (2018) 74 – 82. doi:10.1016/j.applthermaleng.2018.03.056.

[15] F. Valiorgue, A. Brosse, P. Naisson, J. Rech, H. Hamdi, J. M. Bergheau, Emissivity calibration for temperatures measurement using thermography in the context of machining, Applied Thermal Engineering 58 (1) (2013) 321 – 326. doi:10.1016/j.applthermaleng.2013.03.051.

[16] C. Dinc, I. Lazoglu, A. Serpenguzel, Analysis of thermal fields in orthogonal machining with infrared imaging, Journal of Materials Processing Technology 198 (1-3) (2008) 147 – 154. doi:10.1016/j.jmatprotec.2007.07.002.

[17] B. Mller, U. Renz, Time resolved temperature measurements in manufacturing, Measurement 34 (4) (2003) 363–370.

[18] M. Al Huda, K. Yamada, A. Hosokawa, T. Ueda, Investigation of temperature at tool-chip interface in turning using two-color pyrometer, Journal of manufacturing science and engineering 124 (2) (2002) 200–207. doi:10.1115/1.1455641.

[19] J. Artozoul, C. Lescalier, O. Bomont, D. Dudzinski, Extended infrared thermography applied to orthogonal cutting: Mechanical and thermal aspects, Applied Thermal Engineering 64 (1-2) (2014) 441–452.

[20] R. M'Saoubi, H. Chandrasekaran, Investigation of the effects of tool micro-geometry and coating on tool temperature during orthogonal turning of quenched and tempered steel, International Journal of Machine Tools and Manufacture 44 (2004) 213 – 224. doi:10.1016/j.ijmachtools.2003.10.006.

[21] J. Heigel, E. Whitenton, B. Lane, M. Donmez, V. Madhavan, W. Moscoso-Kingsley, Infrared measurement of the temperature at the tool-chip interface while machining ti-6al-4v, Journal of Materials Processing Technology 243 (2017) 123–130. doi:10.1016/j.jmatprotec.2016.11.026.

[22] J. C. Garcia-Gonzalez, W. Moscoso-Kingsley, V. Madhavan, Tool rake face temperature distribution when machining ti6al4v and inconel 718, Procedia Manufacturing 5 (2016) 1369–1381. doi:10.1016/j.promfg.2016.08.107.

[23] P.-J. Arrazola, P. Aristimuno, D. Soler, T. Childs, Metal cutting experiments and modelling for improved determination of chip/tool contact temperature by infrared thermography, CIRP Annals-Manufacturing Technology 64 (1) (2015) 57–60.

[24] D. Soler, T. H. Childs, P. J. Arrazola, A note on interpreting tool temperature measurements from thermography, Machining Science and Technology 19 (1) (2015) 174–181.
[25] M. E. Merchant, Basic mechanics of the metal cutting process, Journal of Applied Mechanics 11 (A) (1944) 168–175.
[26] I. Korkut, M. Donertas, The influence of feed rate and cutting speed on the cutting forces, surface roughness and tool–chip contact length during face milling, Materials & design 28 (1) (2007) 308–312.
[27] A. Simoneau, E. Ng, M. Elbestawi, Grain size and orientation effects when microcutting aisi 1045 steel, CIRP Annals-Manufacturing Technology 56 (1) (2007) 57–60.
[28] T. Obikawa, H. Sasahara, T. Shirakashi, E. Usui, Application of computational machining method to discontinuous chip formation, Journal of Manufacturing Science and Engineering 119 (4B) (1997) 667–674.
[29] T. Obikawa, Y. Takemura, Y. Akiyama, J. Shinozuka, H. Sasahara, Microscopic phase-dependent residual stresses in the machined surface layer of two-phase alloy, Journal of Materials Processing Technology 209 (9) (2009) 4496–4501.
[30] P. Arrazola, A. Villar, D. Ugarte, S. Marya, Serrated chip prediction in finite element modeling of the chip formation process, Machining Science and Technology 11 (3) (2007) 367–390.
[31] A. Iturbe, E. Giraud, E. Hormaetxe, A. Garay, G. Germain, K. Ostolaza, P. Arrazola, Mechanical characterization and modelling of inconel 718 material behavior for machining process assessment, Materials Science and Engineering: A 682 (2017) 441–453.
[32] H. B. Abdelali, C. Claudin, J. Rech, W. B. Salem, P. Kapsa, A. Dogui, Experimental characterization of friction coefficient at the tool–chip–workpiece interface during dry cutting of aisi 1045, Wear 286 (2012) 108–115.
[33] J. Rech, P. Arrazola, C. Claudin, C. Courbon, F. Pusavec, J. Kopac, Characterisation of friction and heat partition coefficients at the tool-work material interface in cutting, CIRP Annals-Manufacturing Technology 62 (1) (2013) 79–82.
[34] M. Saez-de Buruaga, J. Esnaola, P. Aristimuno, D. Soler, T. Björk, P. Arrazola, A coupled eulerian lagrangian model to predict fundamental process variables and wear rate on ferrite-pearlite steels, Procedia CIRP 58 (2017) 251–256.